Distinct regions of *H. pylori's* bactofilin CcmA regulate protein-protein interactions to control helical cell shape

Sophie R Sichel[1, 2], Benjamin P Bratton[3, 4], and Nina R Salama[2 *]

1. Molecular Medicine and Mechanisms of Disease Graduate Program, University of Washington, Seattle, WA, 98195, United States
2. Division of Human Biology, Fred Hutchinson Cancer Center, Seattle, WA, 98109, United States
3. Department of Pathology, Microbiology and Immunology, Vanderbilt University Medical Center, Nashville, TN 37232, United States
4. Vanderbilt Institute for Infection, Immunology and Inflammation, Nashville, TN 37232, United States

Corresponding author *

Key words: Bactofilin / cell shape / cytoskeleton / *H. pylori* / peptidoglycan

Abstract

The helical shape of *H. pylori* cells promotes robust stomach colonization, however, how the helical shape of *H. pylori* cells is determined is unresolved. Previous work identified helical-cell-shape-promoting protein complexes containing a peptidoglycan-hydrolase (Csd1), a peptidoglycan precursor synthesis enzyme (MurF), a non-enzymatic homologue of Csd1 (Csd2), non-enzymatic transmembrane proteins (Csd5 and Csd7), and a bactofilin (CcmA). Bactofilins are highly conserved, spontaneously polymerizing cytoskeletal bacterial proteins. We sought to understand CcmA's function in generating the helical shape of *H. pylori* cells. Using CcmA deletion analysis, *in vitro* polymerization, and *in vivo* co-immunoprecipitation experiments we identified that the bactofilin domain and N-terminal region of CcmA are required for helical cell shape and the bactofilin domain of CcmA is sufficient for polymerization and interactions with Csd5 and Csd7. We also found that CcmA's N-terminal region inhibits interaction with Csd7. Deleting the N-terminal region of CcmA increases CcmA-Csd7 interactions and destabilizes the peptidoglycan-hydrolase Csd1. Using super-resolution microscopy, we found that Csd5 recruits CcmA to the cell envelope and promotes CcmA enrichment at the major helical axis. Thus, CcmA helps organize cell-shape-determining proteins and peptidoglycan synthesis machinery to coordinate cell wall modification and synthesis, promoting the curvature required to build a helical cell.

Introduction

41 *Helicobacter pylori* is a helical-shaped, Gram-negative bacteria that infects more than
42 half of the world's population (Hooi *et al*, 2017). Chronic infection with *H. pylori* can cause
43 gastric ulcers and cancers; approximately 80% of gastric cancer cases are attributed to
44 *H. pylori* infection (de Martel *et al*, 2020). The helical shape of *H. pylori* cells helps
45 establish colonization of the stomach and promotes immunopathology during infection
46 (Martinez *et al*, 2018; Montecucco & Rappuoli, 2001; Sycuro *et al*, 2010; Sycuro *et al*,
47 2012; Yang *et al*, 2019). Multiple proteins have been identified that are essential for the
48 helical shape of *H. pylori* cells, most of which influence the shape and composition of the
49 peptidoglycan (PG) sacculus directly or indirectly (Sycuro *et al.*, 2010; Sycuro *et al*, 2013;
50 Sycuro *et al.*, 2012; Yang *et al.*, 2019).

51 Several cell-shape-determining (Csd) proteins form membrane-spanning protein
52 complexes. Csd5 is a transmembrane protein that binds directly to PG in the periplasm
53 with its SH3 domain and binds to CcmA in the cytoplasm. Csd5 also interacts with ATP
54 synthase and MurF, an essential PG precursor enzyme that catalyzes the final
55 cytoplasmic PG biosynthesis step, independent of interactions with CcmA (Blair *et al*,
56 2018; Hrast *et al*, 2013). Another complex is formed by Csd7, Csd1, and Csd2. Csd7 is
57 a transmembrane protein that stabilizes the PG-hydrolase Csd1, and Csd2, a catalytically
58 inactive homologue of Csd1. Weak interactions between Csd7 and CcmA have been
59 detected by co-immunoprecipitation experiments that include cross-linking reagents
60 followed by mass spectrometry, but whether CcmA, Csd7, and Csd5 are all part of one
61 protein complex is unclear (Yang *et al.*, 2019). CcmA and probes that report on PG
62 synthesis localize to the major helical axis of *H. pylori* cells (regions with a Gaussian

63 curvature value of 5 ±1 μm^{-2} on a helical cell) indicating that CcmA is in the same region
64 of the cell where increased levels of PG synthesis occur (Taylor *et al*, 2020).

65 CcmA is the only bactofilin encoded in the *H. pylori* genome. Bactofilins, a class of
66 highly conserved, spontaneously-polymerizing, cytoskeletal proteins in bacteria, perform
67 a variety of functions (Bulyha *et al*, 2013; El Andari *et al*, 2015; Lin *et al*, 2017; Osorio-
68 Valeriano *et al*, 2019) including modulating cell shape in multiple different bacterial
69 species (Brockett *et al*, 2021; Hay *et al*, 1999; Jackson *et al*, 2018; Koch *et al*, 2011;
70 Sycuro *et al.*, 2010) and morphogenesis of cell appendages (Billini *et al*, 2019; Caccamo
71 *et al*, 2020; Kuhn *et al*, 2010), both of which involve modification or synthesis of PG. But
72 how a cytoplasmic bactofilin influences the PG cell wall in the periplasm is unclear.
73 Bactofilins are identified by the presence of a bactofilin domain (DUF583) which forms a
74 β-helix and is flanked by unstructured terminal regions. The function of the terminal
75 regions and bactofilin domain of bactofilins are debated. It has been proposed that the
76 terminal regions may be involved in modulating polymerization, binding to membranes
77 and/or interacting with other proteins (Deng *et al*, 2019; Kuhn *et al.*, 2010; Vasa *et al*,
78 2015)

79 Here, we performed structure-function analysis to determine how the bactofilin
80 domain and the terminal regions of CcmA contribute to generating the helical shape of *H.*
81 *pylori* cells by evaluating cell morphology, CcmA polymerization and filament bundling,
82 and interaction with known Csd protein interaction partners. Additionally, we identified
83 how protein binding partners impact CcmA localization. We found that polymer bundling
84 and interactions between CcmA and other Csd proteins are responsible for CcmA's ability
85 to pattern the helical shape of *H. pylori* cells and identified that interactions between CcmA

86 and its binding partners modulate CcmA localization and modulate protein stability of the
87 PG-hydrolase Csd1. Together these findings allow us to establish a new model for how
88 *H. pylori*'s helical cell shape is generated. We clarify that CcmA participates in two
89 separate helical-cell-shape-generating protein complexes. Additionally, these studies
90 reveal that bactofilins can influence PG sacculus structure by modulating the protein
91 stability of a PG hydrolase.
92
93 Results
94
95 **CcmA is composed of a bactofilin domain and two short terminal regions**
96 We identified the functional regions of CcmA by aligning the amino acid sequence
97 of CcmA with BacA, a well-studied bactofilin from *C. crescentus* involved in stalk
98 morphogenesis, using Swiss-Model (Waterhouse *et al*, 2018) and found that CcmA is
99 composed of a bactofilin domain (DUF 583) surrounded by two short terminal regions
100 (Figure 1A). The N-terminal region is composed of amino acids 1-17, the bactofilin domain
101 is composed of amino acids 18-118, and the C-terminal region is composed of amino
102 acids 119-136. Deng and colleagues proposed that bactofilins may contain a short
103 membrane binding motif within their N-terminal regions and in CcmA that motif spans
104 amino acids 3-12 (Deng *et al.*, 2019). After identifying the boundaries between the
105 bactofilin domain and the terminal regions of CcmA we used RoseTTAFold (Baek *et al*,
106 2021), a protein structure prediction service that uses deep learning-based modeling
107 methods, to predict the structure of CcmA. RoseTTAFold generated five models of CcmA.
108 In all five, the bactofilin domain forms a three-sided, right-handed β-helix with a left-

handed twist (Figure 1B), the N-terminal region is unstructured, and part of the C-terminal region forms a short α-helix and caps the end of the bactofilin domain (Figure 1C). In four of the five models, the first several amino acids of the N-terminal region interact with the bactofilin domain suggesting that the N-terminal region could potentially block a surface of the bactofilin domain.

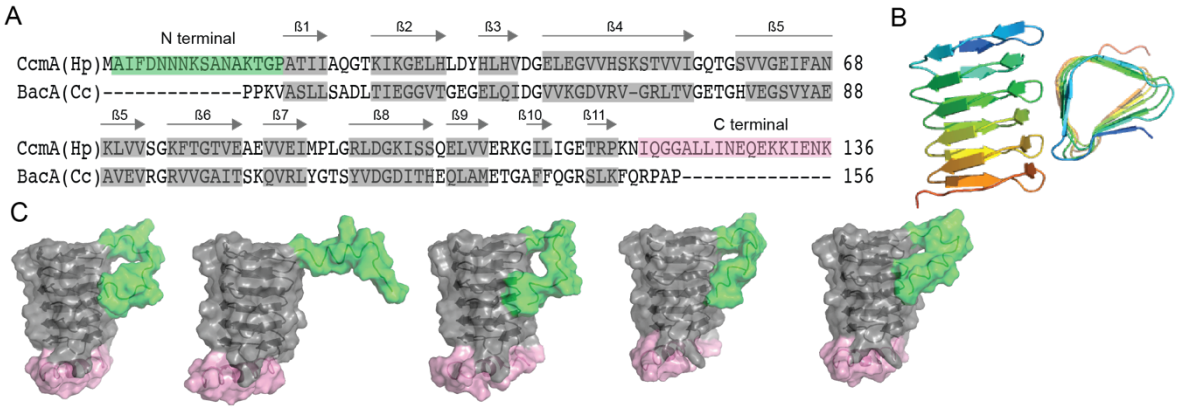

Figure 1- Predicted structure of CcmA. (A) Sequence alignment between BacA from *C. crescentus* and CcmA from *H. pylori* generated with SwissModel, gray boxes indicate β-strands formed in the bactofilin domain, the green box indicates the N-terminal region of CcmA and the pink box indicates the C-terminal region of CcmA. (B) Model of the bactofilin domain of CcmA generated by Robetta which forms a right-handed, 3-sided, triangular β-helix. (C) Five models of CcmA generated in RoseTTAFold displaying the bactofilin domain (gray), N-terminal region (green), and C-terminal region (pink).

126 **The N-terminal region and bactofilin domain are together necessary and sufficient**
127 **to pattern the helical shape of *H. pylori* cells**

128 To identify the role of each domain/region of CcmA we generated *H. pylori* strains that
129 have truncated versions of *ccmA* at the native c*cmA* locus. We generated five strains,
130 one strain missing the N-terminal region (Δ*NT*, missing amino acids 2-17), another strain
131 missing the proposed membrane binding motif within the N-terminus (Δ*MM*, missing
132 amino acids 3-12), a third strain lacking the five amino acids at the end of the N-terminus
133 (Δ*13-17*, lacking amino acids 13-17), a fourth strain missing the C-terminal region (Δ*CT*,
134 missing amino acids 119-136), and lastly, a strain expressing only the bactofilin domain
135 lacking both the N-terminal region and C-terminal region (BD, expressing amino acids 18-
136 118) (Figure 2A). The open reading frames (ORF) of the end of *csd1* and the beginning
137 of *ccmA* overlap by 82 nucleotides (Sycuro *et al.*, 2010), thus to avoid impacting the
138 function of Csd1 by removing several amino acids from the C-terminus when truncating
139 the N-terminus of CcmA, we expressed a second copy of *csd1* at *rd*xA, a locus commonly
140 used for complementation (Smeets *et al*, 2000). In previous work, we confirmed that both
141 CcmA and Csd1 can be individually deleted and complemented back without impacting
142 the expression of the other (Sycuro *et al.*, 2010; Yang *et al.*, 2019).

143 All strains expressed the truncated versions of CcmA measured by Western blotting
144 with an α-CcmA polyclonal antibody, however, in strains lacking the C-terminus (Δ*CT* and
145 BD) we saw much lower signal on the blot (Figure 2B). In follow-up experiments we
146 determined that the α-CcmA polyclonal antibody fails to recognize versions of CcmA
147 lacking the C-terminus (Supplemental Figure 1). We ran a Western blot probed with our
148 polyclonal α-CcmA antibody on purified 6-his WT CcmA and CcmA truncation mutants

149 (Supplemental Figure 2). Although equal concentrations of each purified protein were
150 loaded, the polyclonal α-CcmA antibody poorly recognized versions of CcmA lacking the
151 C-terminal region (Δ*CT* and BD), suggesting that the Δ*CT* and BD proteins are likely
152 expressed in *H. pylori* cells at similar levels to other versions of CcmA but are not robustly
153 recognized by the α-CcmA polyclonal antibody.

154 Next, after confirming that all truncated versions of CcmA were expressed, we
155 assessed the shapes of the cells and found that strains lacking the N-terminal region
156 (Δ*NT* and BD) were indistinguishable from Δ*ccmA* cells (Figure 2 C-D), while cells lacking
157 the C-terminal region of *ccmA* resembled WT cells. Cells that lacked either the putative
158 membrane binding motif (Δ*MM*) or the last five amino acids of the N-terminal region (Δ*13-*
159 *17*) were helical but had slightly different side curvature values than the WT population,
160 suggesting that the N-terminal region of CcmA may have multiple functional regions within
161 it.

162

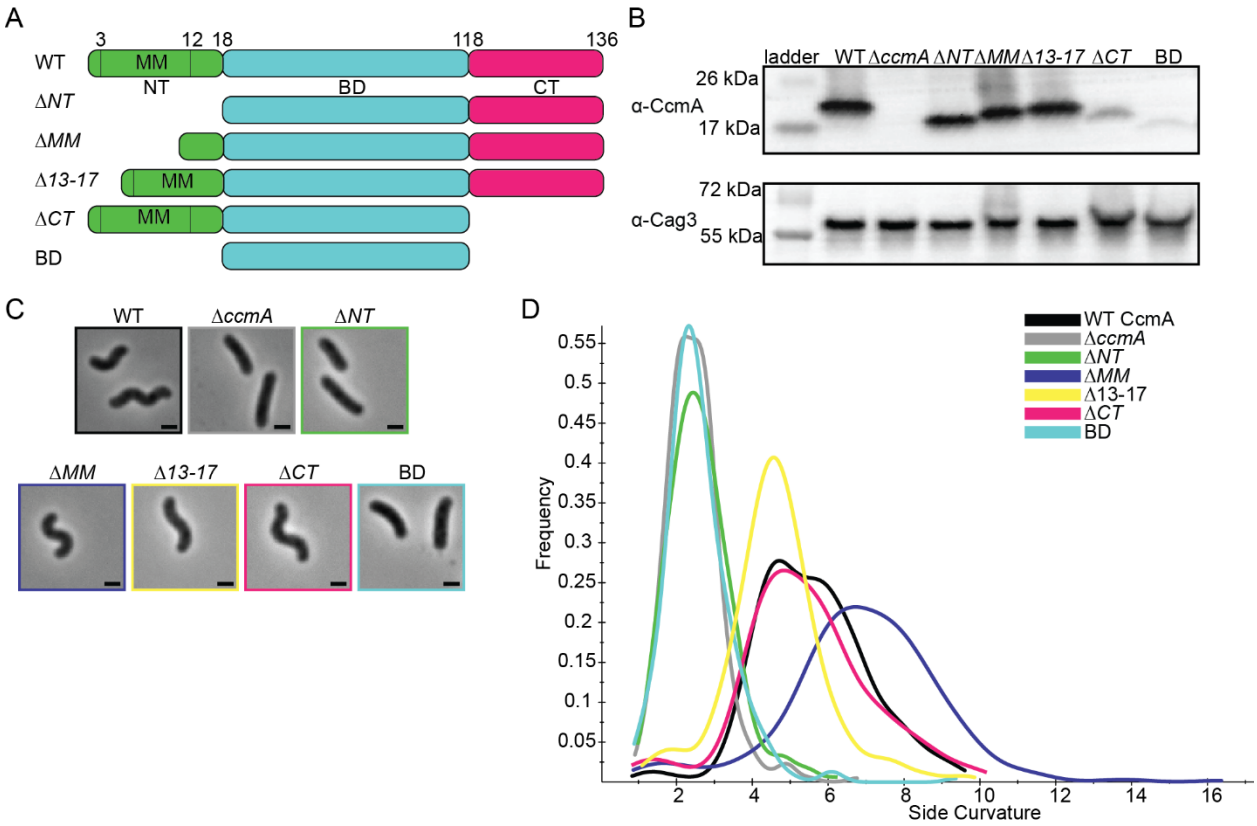

Figure 2- *H. pylori* cells expressing CcmA truncation mutants have different cell shapes. (A) Schematic of CcmA and truncation mutants. The N-terminal region (NT, green), bactofilin domain (BD, cyan), and C-terminal region (CT, pink) are indicated as well as the putative membrane binding motif (MM). (B) Western blot to detect CcmA in whole cell lysates of *H. pylori* strains expressing truncated versions of CcmA probed with α-CcmA polyclonal antibody, and α-Cag3 polyclonal antibody as a loading control. (C) Phase contrast images of *H. pylori* strains expressing truncated versions of CcmA diagramed in panel A, scalebars = 1 μm. (D) Histogram displaying the side curvature of *H. pylori* strains expressing truncated versions of CcmA (WT n= 476 cells, Δ*ccmA* n= 397 cells, Δ*N* n=275 cells, Δ*MM* n= 391 cells, Δ13-17 n=361 cells, Δ*CT* n= 263 cells, BD n=315 cells). Data are representative of two independent biological replicates. Strains used: SSH51A, SSH53A, SSH55A, SSH54A, SSH67A, SSH56B, and SSH57A.

176

177

178 **Circular dichroism spectroscopy reveals that CcmA truncation mutants maintain**
179 **β-strand secondary structure**

180 Circular dichroism (CD) spectroscopy can be used to identify the secondary
181 structure and folding of proteins. Different structural elements have characteristic CD
182 spectra and proteins that consist of β-strands have negative peaks at 216 nm (Greenfield,
183 2006). We sought to identify whether CcmA is composed of β-strands and confirm that
184 our truncated versions of CcmA were still folded correctly, especially considering that in
185 *H. pylori* strains lacking the N-terminal region of CcmA, cells resembled Δ*ccmA* mutants.
186 We recombinantly expressed and purified 6-his CcmA (Supplemental Figure 2) and
187 collected circular dichroism spectra from 200-260 nm at fixed temperatures to identify the
188 secondary structure and measure its thermal stability.

189 CD spectra of WT CcmA and the truncation mutants Δ*NT*, Δ*CT*, and BD at 20 ºC
190 all look very similar; they have the characteristic negative peak at 216 nm indicating β-
191 strand secondary structure (Figure 3A). Together, these data combined with the modeling
192 by RoseTTAFold in Figure 1C suggest that CcmA's bactofilin domain very likely forms a
193 β-helix. In contrast, we also ran CD scans on WT CcmA at 95 ºC and two CcmA point
194 mutants that our group previously studied, I55A and L110S at 20 ºC (Taylor *et al.*, 2020).
195 The CD spectra of both mutants (I55A and L110S) at 20 ºC resemble spectra of melted
196 WT CcmA at 95 ºC (Figure 3B), suggesting that these proteins are not folded. Thus, while
197 CcmA Δ*NT*, BD, I55A, and L110S all have the same cell shape phenotype when
198 expressed in *H. pylori* - loss of helical cell shape - the mechanism differs. In CcmA I55A

199 and L110S, CcmA is not folded and nonfunctional, while in CcmA Δ*NT* and BD, the protein

200 is folded, but loss of the N-terminus causes a loss of helical cell shape.

201

202

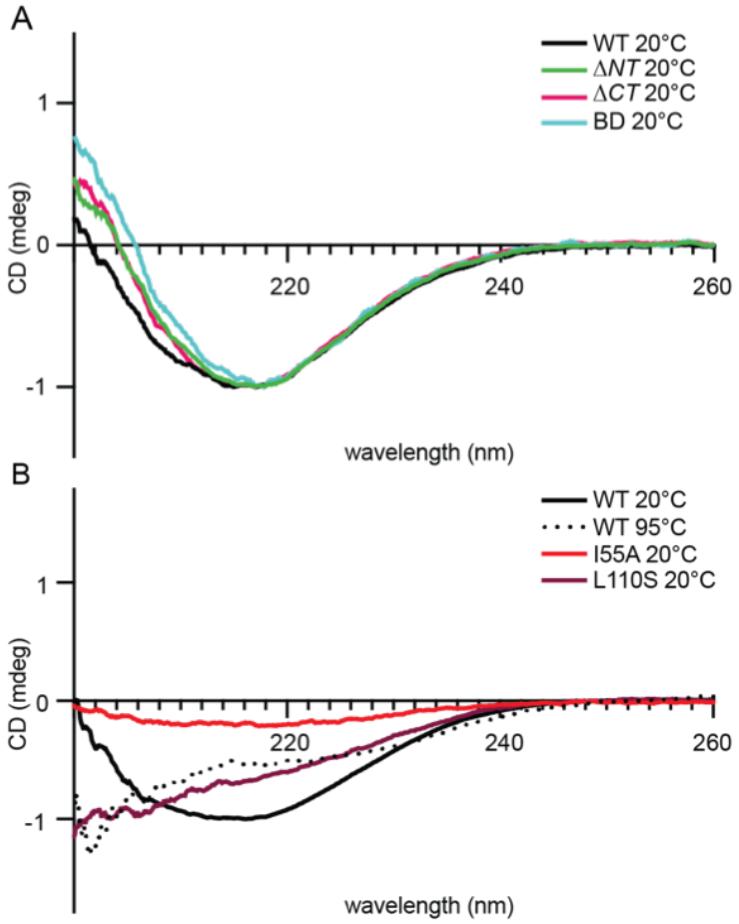

203

204 Figure 3- Circular dichroism spectra of purified 6-his CcmA suggests CcmA is composed

205 of predominantly β-sheets. (A) Circular dichroism spectra of WT and truncated versions

206 of CcmA at room temperature (20 ºC), WT (black), Δ*NT* (green), Δ*CT* (pink), and BD

207 (cyan). (B) Circular dichroism spectra of WT CcmA at room temperature (20 ºC, black),

208 melted (95 ºC, dotted line), and two point mutants (I55A, red and L110S, burgundy).

209

210

211 **The bactofilin domain alone is capable of polymerization; the terminal regions of**
212 **CcmA modulate lateral interactions between CcmA filaments**

213 To identify how each domain/region of CcmA contributes to *in vitro* polymerization
214 we expressed and purified truncated versions of 6-his CcmA and assessed
215 polymerization by negative stain and transmission electron microscopy (TEM). As
216 previously reported (Holtrup *et al*, 2019; Taylor *et al.*, 2020), WT CcmA polymerizes into
217 small filaments that measure on average 3.04 nm (SD= 0.79, n=18) in width. The
218 filaments wrap together to form bundles of approximately 21.34 nm (SD= 4.82, n=24)
219 wide, and form lattice structures (Figure 4 A, G). Δ*NT* formed filaments and bundles which
220 were more homogenous, straighter, and thinner than WT and appear to only contain 2-4
221 filaments each. Δ*NT* failed to form lattice structures (Figure 4B). Δ*MM* resembled WT
222 CcmA, forming filaments and bundles of approximately the same width as WT and formed
223 lattices (Figure 4C, G). Δ*13-17* resembled Δ*NT* (Figure 4D, G), suggesting that amino
224 acids 13-17 are responsible for filament bundling properties of Δ*NT*. Δ*CT* formed bundles
225 that were wider than WT CcmA but failed to form lattices (Figure 4E, G). Lastly, BD formed
226 straight bundles that were narrower than those found in WT samples, and failed to form
227 lattices (Figure 4F, G). These data suggest that the bactofilin domain is sufficient for
228 polymerization of CcmA while the N- and C-terminal regions of CcmA regulate inter-
229 polymer interactions that impact the width of bundles by modulating the number of
230 filaments that form a bundle, and the ability of CcmA to form lattices.

231

232

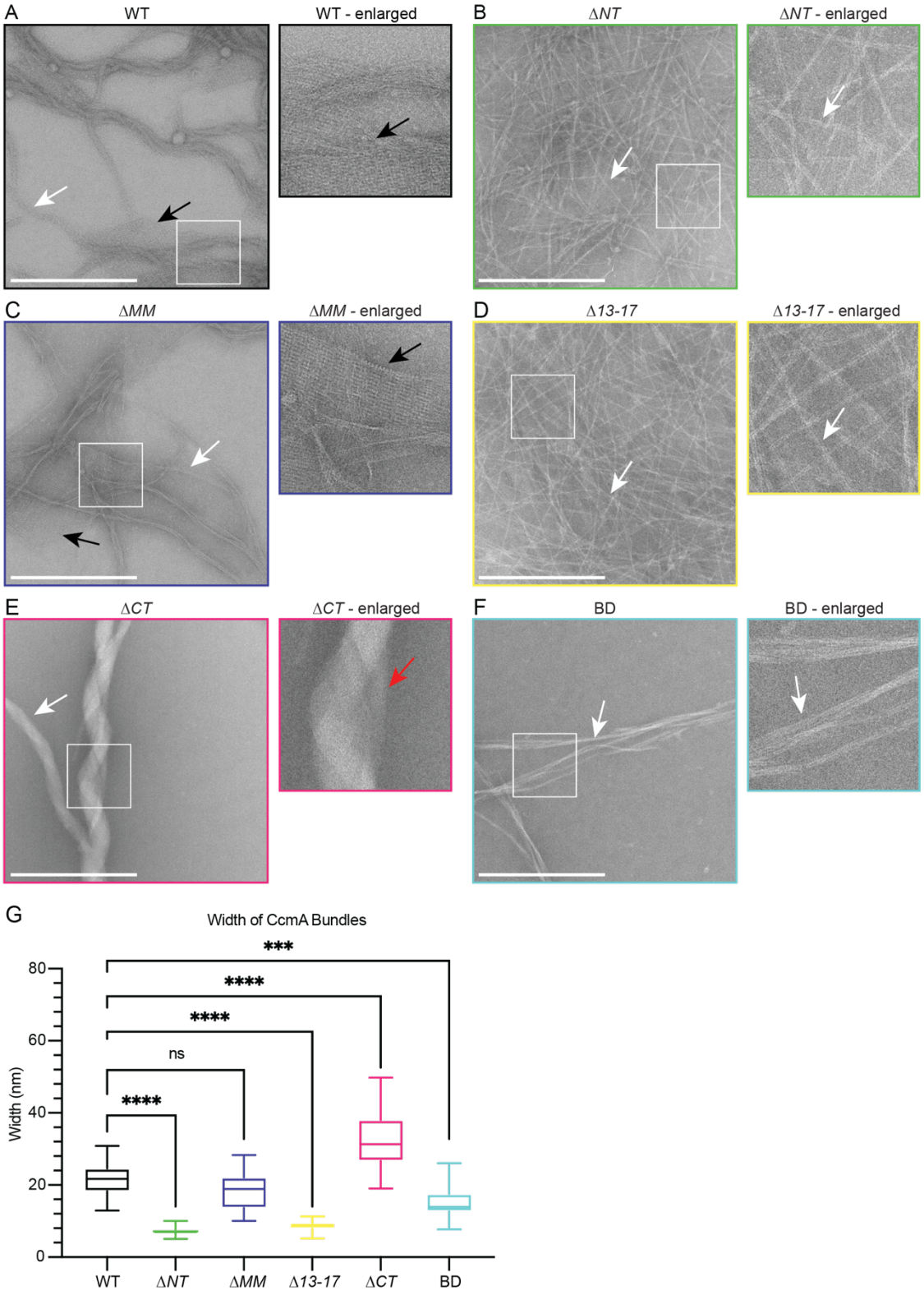
A
WT
WT - enlarged
B
ΔNT
ΔNT - enlarged
C
ΔMM
ΔMM - enlarged
D
Δ13-17
Δ13-17 - enlarged
E
ΔCT
ΔCT - enlarged
F
BD
BD - enlarged
G
Width of CcmA Bundles
Width (nm)
0
20
40
60
80
***
****
****
ns
****
WT
ΔNT
ΔMM
Δ13-17
ΔCT
BD

234 Figure 4- The bactofilin domain of CcmA is sufficient for *in vitro* polymerization while the
235 terminal regions promote lateral polymer interactions. (A-F) TEM of negative stained,
236 purified CcmA, scalebars = 500 nm. White boxes indicate region of micrograph that is
237 enlarged in panel to the right of original. White arrows indicate bundles of CcmA, black
238 arrows indicate lattice structures, red arrow indicates two bundles wrapping around each
239 other. Data are representative of two independent biological replicates. (G) Box and
240 whiskers plot displaying width of purified CcmA bundles and filaments. Median, min, max,
241 25th percentile, and 75th percentile are displayed. One-way ANOVA, Dunnett's multiple
242 comparisons test. ns P>0.5, *** P≤0.001, **** P ≤0.0001. WT n=24, Δ*NT* n=29, Δ*MM*
243 n=25, Δ*13-17* n=31, Δ*CT* n=24, BD n=32.
244
245
246 **CcmA's bactofilin domain mediates interactions with Csd5 and Csd7, and the N-**
247 **terminal region of CcmA inhibits interactions with Csd7**
248 CcmA was previously shown to interact with two Csd proteins, Csd5 and Csd7, by co-
249 immunoprecipitation experiments. Csd5-CcmA interactions were readily detected by co-
250 immunoprecipitation followed by mass spectrometry and by Western blotting. However,
251 Csd7-CcmA interactions could only be detected when a cross-linking reagent was
252 included in co-immunoprecipitation experiments and mass spectrometry was used to
253 detect CcmA, suggesting that Csd7-CcmA interactions are weak or potentially transient
254 (Blair *et al.*, 2018; Yang *et al.*, 2019). To probe how each region of CcmA contributes to
255 interactions with Csd5 and Csd7, we performed co-immunoprecipitation experiments
256 followed by Western blotting. Strains were generated that expressed truncated versions

257 of *ccmA* at the native *ccmA* locus, *csd1* at the *rdxA* locus as described earlier, and either
258 *csd5-2X-FLAG* or *csd7-3X-FLAG* at their native loci. We immunoprecipitated either Csd5-
259 FLAG or Csd7-FLAG with α-FLAG agarose beads, then performed Western blotting and
260 probed with the α-CcmA polyclonal antibody to identify whether the truncated versions of
261 CcmA could still co-purify. When we immunoprecipitated Csd5-FLAG, all mutant versions
262 of CcmA were detected by Western blotting of the IP fractions, except for the Δ*CT* mutant
263 (Figure 5A), though it is likely that this mutant can still interact with Csd5-FLAG. Earlier
264 we identified that the C-terminal region of CcmA is required for robust detection by our α-
265 CcmA polyclonal antibody (Supplemental Figure 1) and here, the BD mutant interacts
266 with Csd5. Additionally, we tagged WT CcmA, Δ*CT* and BD with a HaloTag in *H. pylori* at
267 the native *ccmA* locus and performed a co-immunoprecipitation experiment to detect
268 interactions with Csd5-FLAG (Supplemental Figure 3). We found that both Δ*CT*-HaloTag
269 and BD-HaloTag were expressed at comparable levels as CcmA-HaloTag and could be
270 pulled down by Csd5-FLAG. These three pieces of evidence lead us to conclude that the
271 Δ*CT* mutant can interact with Csd5, suggesting that only the bactofilin domain is required
272 for interactions between CcmA and Csd5-FLAG.

273 When we immunoprecipitated Csd7-FLAG we found that, as previously reported
274 (Yang *et al.*, 2019), WT CcmA was not able to be detected in the IP fractions by Western
275 blotting above background levels. However, versions of CcmA lacking the N-terminal
276 region were robustly co-purified by Csd7 (Figure 5B) suggesting that the N-terminal
277 region inhibits WT CcmA from being co-immunoprecipitated by Csd7-FLAG. Together
278 these data suggest that the bactofilin domain of CcmA mediates interaction with Csd5
279 and Csd7, the N-terminal region of CcmA inhibits interaction with Csd7, and versions of

280 CcmA lacking the C-terminal region are expressed at comparable levels to WT CcmA
281 although they are not recognized as robustly by the α-CcmA polyclonal antibody.
282
283

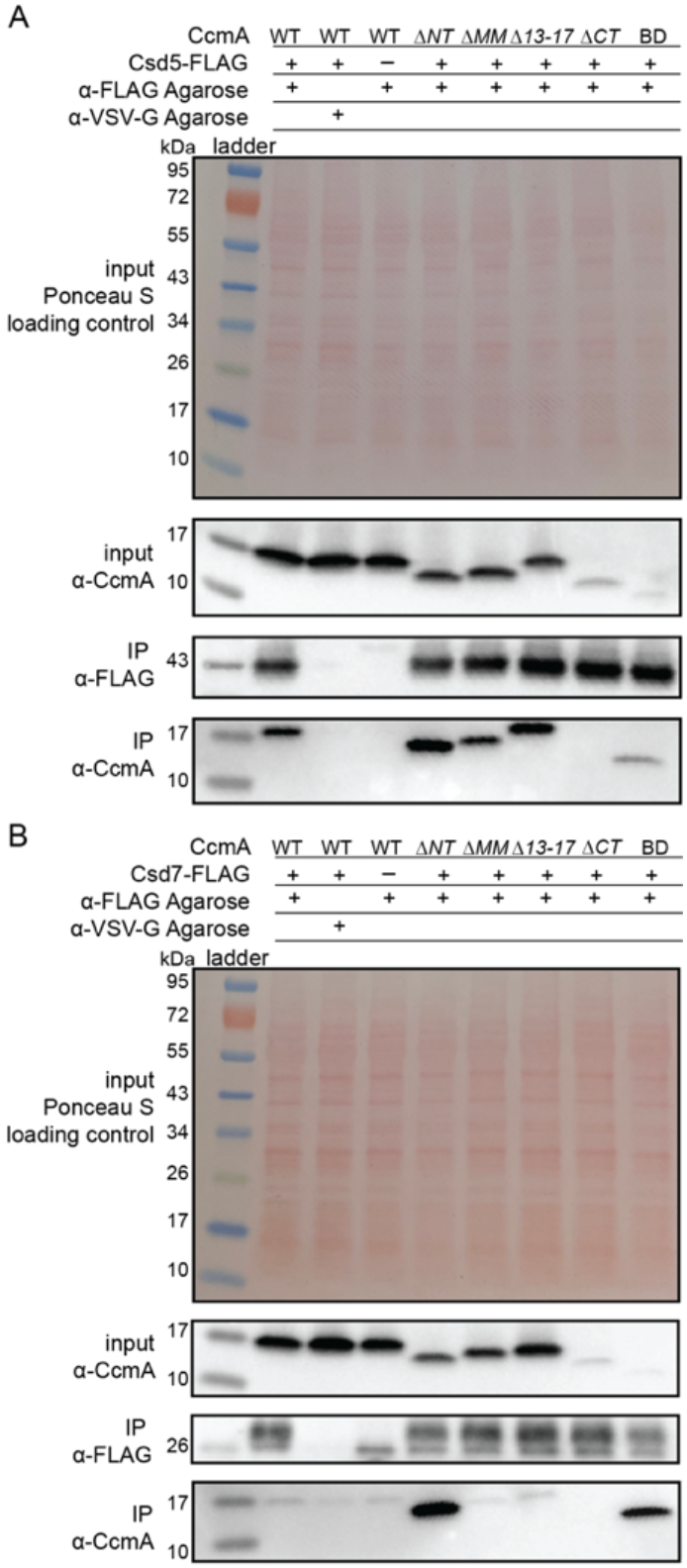
A
CcmA WT WT WT ΔNT ΔMM Δ13-17 ΔCT BD
Csd5-FLAG + + − + + + + +
α-FLAG Agarose + + + + + + +
α-VSV-G Agarose +
kDa ladder
95
72
55
43
34
26
17
10
input
Ponceau S
loading control
input
α-CcmA
IP
α-FLAG
IP
α-CcmA
B
CcmA WT WT WT ΔNT ΔMM Δ13-17 ΔCT BD
Csd7-FLAG + + − + + + + +
α-FLAG Agarose + + + + + + +
α-VSV-G Agarose +
kDa ladder
95
72
55
43
34
26
17
10
input
Ponceau S
loading control
input
α-CcmA
IP
α-FLAG
IP
α-CcmA

285 Figure 5 – The bactofilin domain interacts with Csd5 and Csd7, and the N-terminal region
286 inhibits Csd7 binding to CcmA. Co-immunoprecipitation experiments to probe Csd5-2x-
287 FLAG-CcmA interactions (A) and Csd7-3x-FLAG-CcmA interactions (B) in *H. pylori* cells
288 are shown. Top row: Ponceau S staining of input fractions. Second row: Western blot
289 probed with α-CcmA polyclonal antibody of input fractions. Third row: Western blot probed
290 with α-FLAG monoclonal antibody of immunoprecipitation (IP) fractions. Bottom row:
291 Western blot probed with α-CcmA polyclonal antibody of IP fractions. Data shown are
292 representative of data from three independent biological replicates. Strains used:
293 KHB157, LSH100, SSH59A, SSH58A, SSH68A, SSH60A, SSH65A, DCY71, SSH79A,
294 SSH78A, SSH82, SSH80A, and SSH81B.
295
296
297 **Increased CcmA-Csd7 interactions preclude Csd1-Csd7 interactions, resulting in**
298 **decreased Csd1 expression**
299 After discovering that the N-terminal region of CcmA could inhibit interactions with Csd7
300 and that Δ*NT* CcmA was readily co-purified by Csd7, we reasoned that Δ*NT* CcmA could
301 be binding to Csd7 and reducing its capacity to stabilize Csd1, causing decreased levels
302 of Csd1 expression. This hypothesis was bolstered by the finding that Δ*csd7,* Δ*csd1*, and
303 Δ*NT* cells all share the same curved rod shape phenotype. To test this hypothesis, we
304 assayed Csd1 expression by Western blotting and probing with an α-Csd1 polyclonal
305 antibody in whole cell lysates of the *H. pylori* strain lacking the N-terminal region of *ccmA*.
306 As discussed previously, this strain express two copies of Csd1; there is an extra copy of
307 *csd1* at *rdxA* which was added to account for potentially impacting Csd1's function when

308 truncating *ccmA* (the ORF of the end of *csd1* and the beginning of *ccmA* overlap by 82
309 nucleotides). Strikingly, we found that in the strain lacking the N-terminal region (Δ*NT*)
310 Csd1 levels are lower than in a strain expressing WT CcmA (Figure 6 A-B). After
311 identifying that Csd1 levels were depleted when the N-terminal region of CcmA was
312 missing, we sought to identify if Csd7-Csd1 interactions were diminished when Csd7-
313 CcmA interactions increased. We performed Western blotting and probed for Csd1 levels
314 in the samples we collected during our Csd7-FLAG co-immunoprecipitation experiments
315 (Figure 5B). We found that in *H. pylori* strains lacking the N-terminal region of CcmA,
316 Csd7-Csd1 interactions are decreased in comparison to when WT CcmA is expressed.
317 Suggesting that when the N-terminal region of CcmA is deleted CcmA-Csd7 interactions
318 increase and inhibit Csd7 from stabilizing Csd1, causing decreased Csd1 levels. Our data
319 suggest that Csd1 stability is indirectly regulated by CcmA via Csd7.
320
321

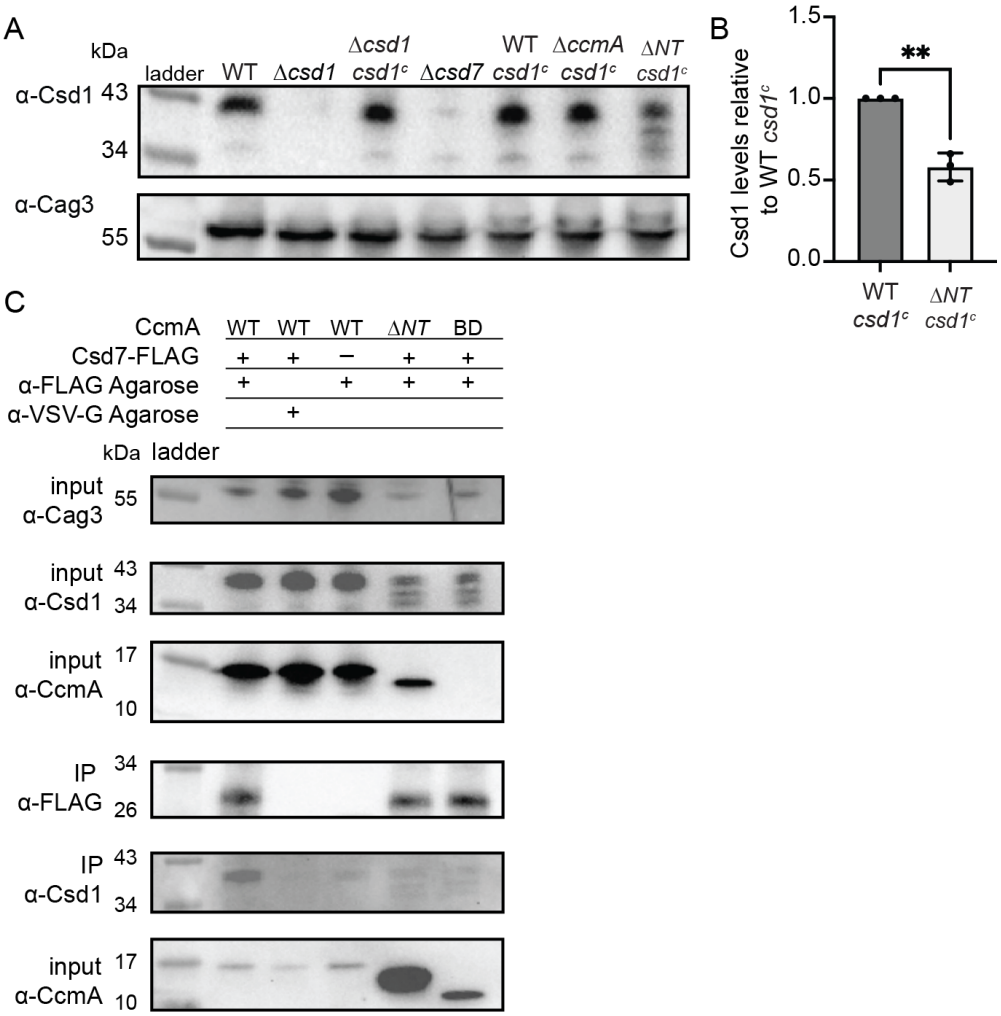

Figure 6- Csd1 expression is diminished when the N-terminal region of CcmA is deleted due to increased Csd7-CcmA interactions that preclude Csd7-Csd1 interactions. (A) Western blot of whole cell extracts probed with α-Csd1 polyclonal antibody showing expression of Csd, α-Cag3 polyclonal antibody was used as a loading control. Strains with "csd1^{c}" indicate an extra copy of *csd1* was added at the *rdxA* locus. Data shown are representative of data from three independent biological replicates. (B) Quantification Csd1 levels in the ccmA Δ*N*T strain relative to the WT *csd1^{c}*. Relative signal was calculated by dividing Csd1 signal by Cag3 signal for each replicate, then the data was normalized by dividing it by the value from the WT *csd1^{c}* strain from the same experiment.

332 Data are pooled from three independent biological replicates. Unpaired t test, ** P≤0.001.
333 (C) Co-immunoprecipitation experiments to probe Csd1 levels in relation to Csd7-3x-
334 FLAG-CcmA interactions in *H. pylori* cells are shown. Top row: Western blot of input
335 fractions probed with α-Cag3 polyclonal antibody as loading control. Second row:
336 Western blot of input fractions probed with α-Csd1 polyclonal antibody. Third row:
337 Western blot of input fractions probed with α-CcmA polyclonal antibody. Fourth row:
338 Western blot probed with α-FLAG monoclonal antibody of immunoprecipitation (IP)
339 fractions to detect Csd7-FLAG. Fifth row: Western blot probed with α-Csd1 polyclonal
340 antibody of IP fractions. Bottom row: Western blot probed with α-CcmA polyclonal
341 antibody of IP fractions. Data shown are representative of data from two independent
342 biological replicates. Strains used: LSH100, LSH113, LSH121, DCY26, SSH51A,
343 SSH53A, SSH55A, DCY71, SSH79A, and SSH81B.
344
345
346 **CcmA requires binding partners for proper localization to the major helical axis**
347 It has been hypothesized that bactofilins are able to interact with the cell envelope
348 directly and sense specific curvature values. To address whether binding partners are
349 required to direct CcmA to the cell envelope, we first engineered an *H. pylori* strain we
350 could use to visualize CcmA. We engineered a strain with *ccmA-HaloTag* at the native
351 *ccmA* locus and a second copy of WT *ccmA* at *rdxA*. We found that cells that expressed
352 CcmA-HaloTag as the sole copy of CcmA were still helical but had slightly lower side
353 curvature than WT cells; adding a second copy of *ccmA* at *rdxA* generated cells with side
354 curvature more similar to WT cells (Supplemental Figure 4). To identify whether CcmA is

355 capable of localizing to the cell envelope at its preferred curvature alone or whether
356 localization is mediated by a binding partner, we deleted *csd5* and *csd7* individually and
357 together in our *ccmA-HaloTag* strain. As an additional control we deleted *csd6* in the
358 *ccmA-HaloTag* strain. Csd6 is a peptidoglycan carboxypeptidase that does not appear to
359 interact with CcmA, Csd5, or Csd7 (Blair *et al.*, 2018; Sycuro *et al.*, 2013; Yang *et al.*,
360 2019). Similar to Δ*csd5* mutants, Δ*csd6* mutants show a straight rod shape phenotype.
361 We fixed and permeabilized cells, then labeled CcmA-HaloTag with a fluorescent ligand
362 (JF-549) that binds to HaloTag and counterstained with fluorescent wheat germ agglutinin
363 (WGA), which binds to PG, to label the cell envelope. We collected images of hundreds
364 of cells from each population using 3D structured illumination microscopy (SIM) and used
365 software previously described to generate 3D reconstructions of individual cells from the
366 WGA channel and calculate the Gaussian curvature at each point on the cell surface.
367 Then we performed analysis to identify how much CcmA-HaloTag signal was at the cell
368 envelope versus in the center of cells, and curvature enrichment analysis to investigate
369 whether CcmA-HaloTag is enriched or depleted at specific Gaussian curvature values
370 (Bratton *et al*, 2019; Taylor *et al.*, 2020).

371 In WT cells, we found that CcmA-HaloTag signal is present as foci and small arcs
372 that colocalize with the cell envelope (white signal) and there were some foci in the center
373 of the cell (Figure 7A top row). The CcmA-HaloTag signal closely resembled what we saw
374 when we visualized CcmA-FLAG by immunofluorescence in previous work (Taylor *et al.*,
375 2020). In cells lacking *csd6*, we found that CcmA-HaloTag signal is present at the cell
376 envelope and there are some foci in the center of cells (Figure 7A second row). In cells
377 lacking *csd7*, cells are slightly curved and CcmA-HaloTag signal colocalizes with the cell

378 envelope, however there are also some foci in the center of the cell (Figure 7A third row).
379 In cells lacking *csd5*, there appears to be more CcmA-HaloTag signal in the center of
380 cells than associated with the cell envelope (Figure 7A fourth row). In cells lacking both
381 *csd5* and *csd7*, we found that the cell shape resembles a Δ*csd7* mutant, however, there
382 appears to be more CcmA-HaloTag signal in the center of the cells than in the Δ*csd7*
383 mutant, similar to the Δ*csd5* mutant (Figure 7A bottom row).

384 To quantify how much CcmA-HaloTag signal was associated with the cell envelope
385 as compared to the amount of CcmA-HaloTag found in the center of the cells, we
386 developed a method to measure the amount of CcmA-HaloTag signal that colocalized
387 with the cell surface as we computationally generated sequential cell surface shells with
388 smaller or larger diameters (Figure 7B and Supplemental Figure 4C-D). We used the
389 fluorescent WGA channel which labels the PG cell wall to generate the cell surface. As
390 we computationally shrink the cell surface (X decreases), we observe the relative
391 concentration of WGA and CcmA-HaloTag signal with respect to the position of the cell
392 surface. In both a WT and Δ*csd5* cell the WGA signal peaks at X=0 nm where the PG cell
393 wall is located within the periplasm. In WT cells, CcmA-HaloTag signal peaks near -50
394 nm from the PG cell wall and declines further to the inside of the cell. Based on cryo-
395 electron tomography data, an approximate distance of 50 nm from the PG cell wall to the
396 cytoplasm in *H. pylori* is expected (Asmar *et al*, 2017; Chang *et al*, 2018; Kuhn *et al.*,
397 2010; Lu *et al*, 2022; Qin *et al*, 2017). In contrast, in a Δ*csd5* cell, the HaloTag-CcmA
398 signal peaks near -100 nm from the cell surface and continues to be high even as the
399 surface of interest approaches center of the cell (approximately -300 nm), indicating that
400 more CcmA-HaloTag signal is found near the center of the cell in Δ*csd5* cells than in WT

401 cells. When we performed the same analysis on the entire populations of cells (292 WT
402 and 326 Δ*csd5*), we found that while the overall trends were the same as when we
403 analyzed individual cells, there was a lot of variability in the WT cell population. The
404 variability of the WT population arises because many WT cells have both a population of
405 CcmA-HaloTag at the cell envelope (peak at -50 nm) and in the center of the cell that
406 causes a broader left tail in the population level data (Supplemental figure 4C-D). In
407 contrast, the *Δcsd5* population level signal peak is broader and shifted towards the center
408 of the cell (-80 nm). Thus, Csd5 is required for CcmA to localize to the cell envelope.

409 To identify where CcmA-HaloTag signal that is at the cell surface is in relation to
410 cell curvature, we calculated the Gaussian curvature values of all cell surfaces
411 represented in the populations. WT cells (which are helical) have a larger range of
412 Gaussian curvature values on their cell surfaces (Figure 7 C-D) compared to all other
413 shape mutants. Interestingly, although all shape mutants are not helical, they do display
414 different surface Gaussian curvature distributions and Δ*csd7* and Δ*csd5/7* populations
415 look nearly identical, suggesting that Δ*csd5/7* double mutants resemble the shape of a
416 Δ*csd7* mutant.

417 In WT cells, CcmA-HaloTag is enriched at the major helical axis (Gaussian
418 curvature value of 5 ±1 μm^{-2} (Taylor *et al.*, 2020)); enrichment peaks at +3.35 μm^{-2} to
419 +5.31 μm^{-2} Gaussian curvature and is depleted at Gaussian curvature values lower than
420 +0.97 μm^{-2} and higher than +6.67 μm^{-2}. These data are consistent previous experiments
421 where CcmA-FLAG was detected by immunofluorescence (Taylor *et al.*, 2020). In
422 contrast, in all other strains, CcmA-HaloTag is depleted at regions of Gaussian curvature
423 where CcmA-Halotag is enriched in WT cells (+3.35 μm^{-2} to +5.31 μm^{-2}) although those

Gaussian curvature values are still present in all cell-shape-mutant populations (Figure 7 E-F). In Δ*csd6* and Δ*csd7* mutants, CcmA-HaloTag is enriched at negative Gaussian curvature values. In Δ*csd6* mutants, enrichment peaks at and continues to be enriched at all values lower than +0.11 μm^{-2} Gaussian curvature (to -4 μm^{-2} Gaussian curvature). In Δ*csd7* mutants, CcmA-HaloTag enrichment peaks at +0.15 μm^{-2} and is enriched at all values below +0.15 μm^{-2} (to -5.4 μm^{-2} Gaussian curvature), (Figure 7 E). In contrast to Δ*csd6* and Δ*csd7* mutants, in Δ*csd5* mutants, CcmA-HaloTag is depleted at negative Gaussian curvature values (Figure 7 F). Interestingly, in a Δ*csd5/7* double mutant, the CcmA-HaloTag enrichment pattern mirrors the Δ*csd5* mutant enrichment pattern. In Δ*csd5* mutants CcmA-HaloTag is enriched at Gaussian curvature values from -1.18 μm^{-2} to +2.5 μm^{-2} and has a peak enrichment at +0.68 μm^{-2}, CcmA-HaloTag is depleted at all other values of Gaussian curvature. In a Δ*csd5/7* double mutant CcmA-HaloTag is enriched at Gaussian curvatures of -0.99 μm^{-2} to +3.46 μm^{-2} and peaks at +0.85 μm^{-2}, CcmA-HaloTag is depleted at all other values of Gaussian curvature. Suggesting that when helical cell shape is disrupted but Csd5 is present (in a Δ*csd6* or Δ*csd7* strain), CcmA localizes to regions of negative Gaussian curvature instead of the major helical axis and that Csd5, not Csd7, modulates CcmA localization.

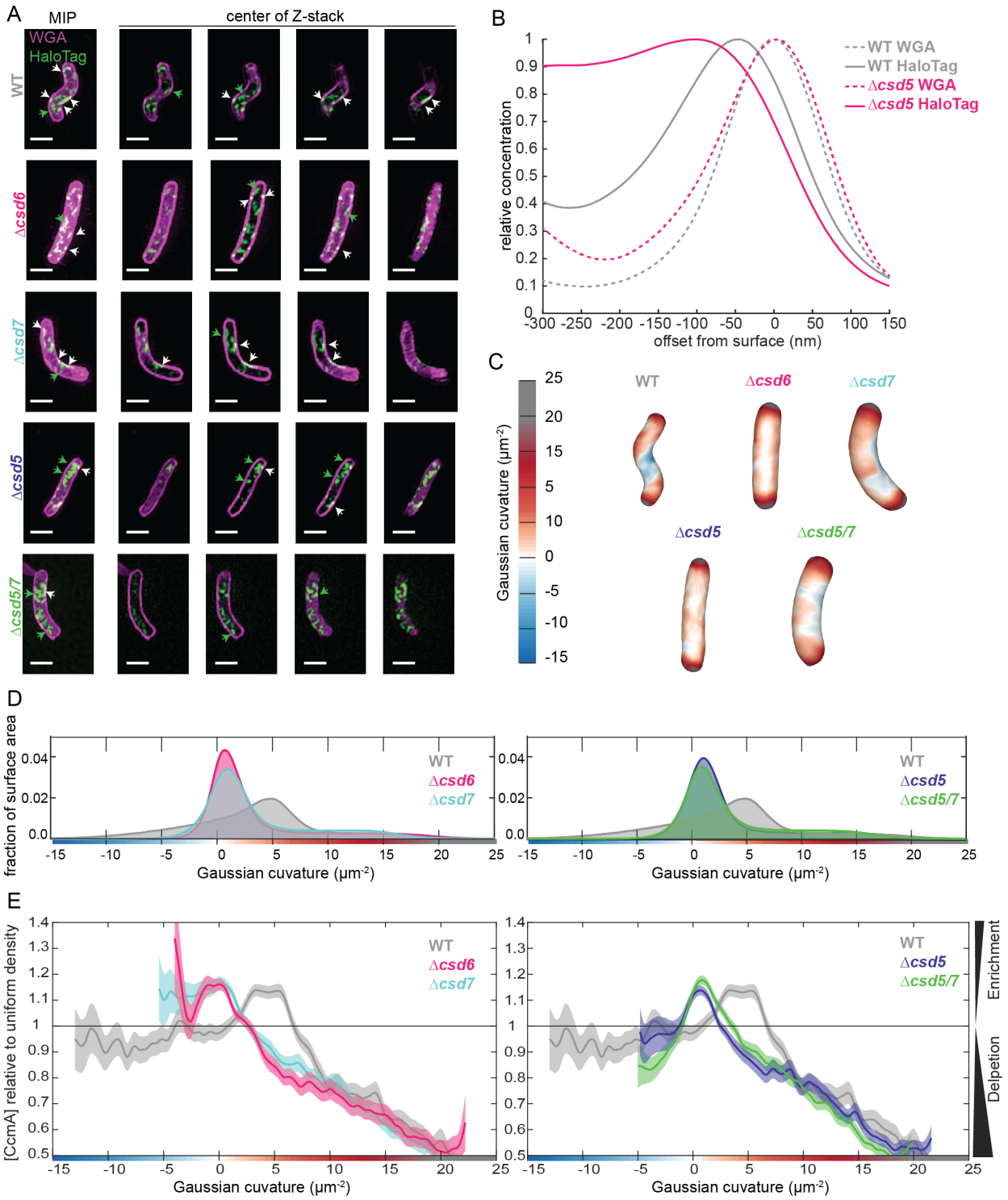

443

444 Figure 7- Csd5 is required for CcmA-HaloTag to localize to the cell envelope at the major

445 helical axis. (A) Maximum intensity projections (MIP) and frames from Z-stacks of *H. pylori*
446 cells labeled with WGA to label the cell wall (magenta) and JF549 ligand to label CcmA-
447 HaloTag (green), pixels are white where the two signals co-localize. Green arrows
448 indicated cytoplasmic CcmA-HaloTag. White arrows indicate CcmA-HaloTag signal that
449 colocalizes with the cell envelope. Scalebars = 1 μm. (B) Representative plots displaying
450 the relative concentration of HaloTag-CcmA and WGA signal from one WT and one Δ*csd5*
451 cell at the cell surface (X=0) and at computationally generated cell surfaces that are inside
452 (X<0) and outside (X>0) of the cell surface. (C) Representative *H. pylori* cells from each
453 population with Gaussian curvature values mapped on the cell surface. (D-E) Top,
454 histogram of Gaussian curvature of cell surfaces of each population. Bottom, surface
455 Gaussian curvature enrichment of relative concentration of CcmA signal in each
456 population where 1=uniform concentration of CcmA, shaded regions indicate SEM. In
457 panels C-F, WT n=292, Δ*csd6* n=264 cells, Δ*csd7* n=355, Δ*csd5* n=326, Δ*csd5/7* n=523.
458 Strains used: SSH39B, SSH49A, SSH50A, JS09, and SSH70A.
459
460

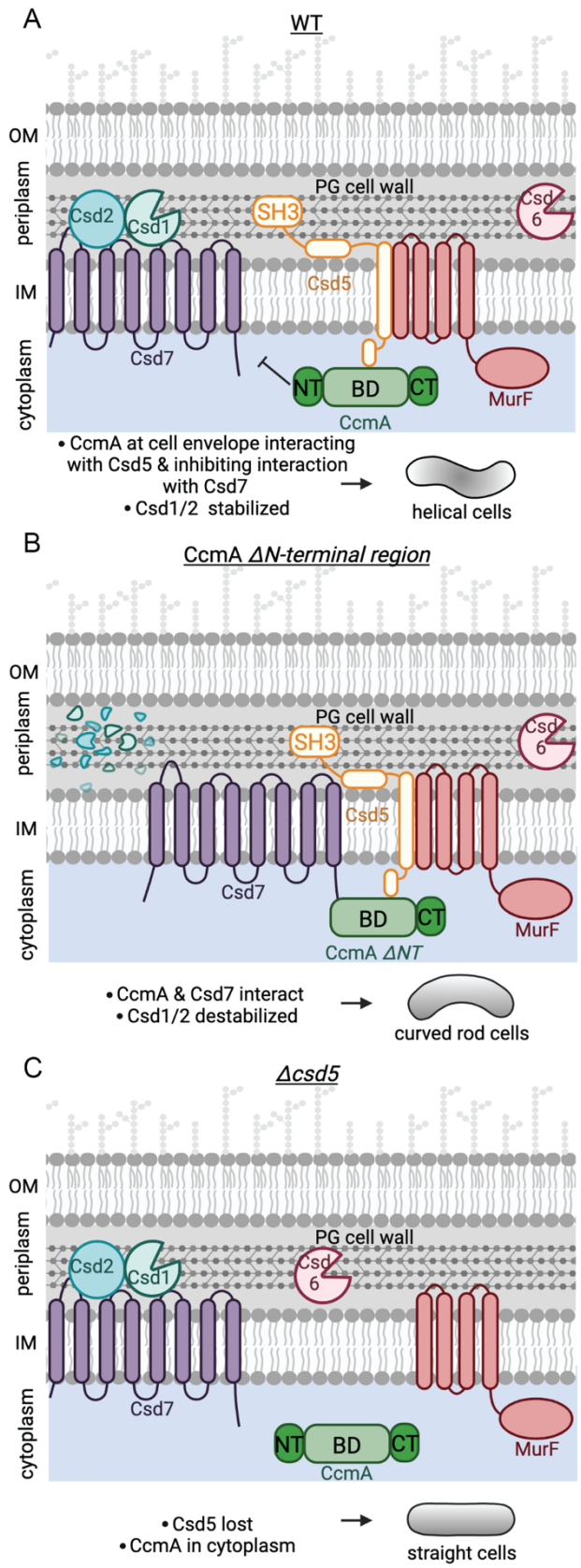
A
WT
OM
periplasm
IM
cytoplasm
PG cell wall
Csd2
Csd1
SH3
Csd 6
Csd5
Csd7
NT
BD
CT
CcmA
MurF
• CcmA at cell envelope interacting with Csd5 & inhibiting interaction with Csd7
• Csd1/2 stabilized
helical cells
B
CcmA ΔN-terminal region
OM
periplasm
IM
cytoplasm
PG cell wall
SH3
Csd 6
Csd5
Csd7
BD
CT
CcmA ΔNT
MurF
• CcmA & Csd7 interact
• Csd1/2 destabilized
curved rod cells
C
Δcsd5
OM
periplasm
IM
cytoplasm
PG cell wall
Csd2
Csd1
Csd 6
Csd7
NT
BD
CT
CcmA
MurF
• Csd5 lost
• CcmA in cytoplasm
straight cells

462 Figure 8- Schematic depicting CcmA's role in the helical cell shape complexes. There are
463 two protein complexes, one containing Csd5, MurF, and CcmA, and another containing
464 Csd7, Csd1, and Csd2. (A) In WT cells, Csd5 recruits WT CcmA to the cell envelope via
465 CcmA's bactofilin domain. The N-terminal region of CcmA inhibits interaction with Csd7,
466 allowing Csd1 to function and excluding Csd1 from the CcmA-Csd5-MurF complex. (B)
467 In cells expressing CcmA Δ*NT,* Csd5 recruits Δ*NT* CcmA to the cell envelope via CcmA's
468 bactofilin domain. The bactofilin domain of CcmA binds to Csd7, inhibiting Csd7 from
469 stabilizing Csd1. (C) When Csd5 is absent, CcmA cannot localize to the cell envelope,
470 MurF is not directed to a particular location. OM = outer membrane, IM =inner membrane.
471 This figure was created using Biorender.com.
472
473
474 Discussion
475 The PG sacculus is what ultimately controls the shape of bacterial cells and it has
476 been hypothesized that modification of PG crosslinking generates curvature and twist of
477 the sacculus (Huang *et al*, 2008; Sycuro *et al.*, 2010). In *H. pylori*, when the cytoplasmic
478 bactofilin CcmA is lost, cells lose their helical shape and the PG muropeptide composition
479 is altered (Sycuro *et al.*, 2010). Interestingly, Δ*csd1*, Δ*csd2*, Δ*csd7*, and Δ*ccmA* mutants
480 all share the same curved rod phenotype and PG muropeptide composition, suggesting
481 that CcmA may regulate Csd1 activity, however prior to this work there was not a clear
482 mechanism linking CcmA and Csd1 activity (Sycuro *et al.*, 2010; Yang *et al.*, 2019). Past
483 work identified that CcmA interacts with the transmembrane protein Csd5 (which binds
484 directly to PG) and may interact weakly with Csd7. Additionally, CcmA localizes to the

485 major helical axis of *H. pylori* cells where rates of PG synthesis are increased (Blair *et al.*,
486 2018; Taylor *et al.*, 2020; Yang *et al.*, 2019). In this study, we identified several new
487 mechanisms that clarify how CcmA regulates the helical cell shape of *H. pylori* by
488 modulating interactions with Csd5 and Csd7.

489 First, we identified that the N-terminal region of CcmA and the bactofilin domain
490 are required for helical cell shape, but that the C-terminal region was not required. Next,
491 in co-immunoprecipitation experiments, we found that the bactofilin domain of CcmA
492 interacts with Csd5 and Csd7 and the N-terminal region inhibits the bactofilin domain from
493 interacting with Csd7. When the N-terminal region of CcmA is removed, the bactofilin
494 domain of CcmA binds to Csd7 and Csd1 levels are depleted, providing the first potential
495 mechanism by which CcmA regulates Csd1.

496 Next, we identified that when other cell-shape-determining genes are deleted,
497 CcmA can no longer localize to the major helical axis of the cell (Gaussian curvature value
498 of 5 ±1 μm^{-2} (Taylor *et al.*, 2020)) suggesting that CcmA is directed to its preferred location
499 by a binding partner and is not capable of localizing to or sensing cell envelope curvature
500 on its own. Loss of Csd5 causes substantially less CcmA to localize to the cell envelope,
501 instead CcmA accumulates in the center of cells. The CcmA signal that does co-localize
502 with the cell envelope in Δ*csd5* and Δ*csd5/7* cells is enriched near zero Gaussian
503 curvature, and is depleted at all other Gaussian curvature values. When *csd6* or *csd7* are
504 deleted, CcmA localizes to regions of negative Gaussian curvature. These data suggest
505 that Csd5 recruits CcmA to the cell envelope. If helical cell shape is disrupted (due to loss
506 of another cell shape protein) while Csd5 is still present, Csd5 directs CcmA to regions of
507 negative Gaussian curvature. Additionally, the finding that CcmA localization phenotypes

508 are the same in a Δ*csd5* mutant and a Δ*csd5/7* double mutant suggest that Csd5, not
509 Csd7, controls CcmA localization. These results also support the hypothesis that there
510 are two helical-cell-shape-generating protein complexes, one containing Csd5 and one
511 containing Csd7, and that CcmA may regulate interactions between them (Figure 8).

512 Using what we have learned in this study, we can build a new model of the protein
513 complexes that pattern the helical shape of *H. pylori* cells. In one protein complex, CcmA's
514 bactofilin domain interacts with the cytoplasmic N-terminal region of the transmembrane
515 protein Csd5 directing CcmA to the cell envelope. Csd5 brings MurF and PG precursors
516 to the same region of the cell envelope for new PG to be inserted into the cell wall (Figure
517 8). CcmA's N-terminal region inhibits interaction of CcmA's bactofilin domain with allows
518 Csd7 to stabilize Csd1. When the N-terminus of CcmA is removed, interactions between
519 Csd7 and CcmA are stabilized and Csd1 is no longer detected in the Csd7 complex. Prior
520 work had shown that Csd1 protein cannot be detected in a Δ*csd7* mutant, suggesting
521 Csd7 binding to Csd1 stabilizes this PG hydrolase. Steady state levels of Csd1 are
522 depleted in the *ccmA ΔNT* mutant suggesting that Csd7 cannot simultaneously interact
523 with Csd1 and CcmA. Thus, CcmA regulates Csd1 activity (cleaving tetra-pentapeptide
524 crosslinks) spatially or temporally in relation to Csd5 and MurF to organize PG
525 modification and insertion. Our work raises the question of how Csd5 localizes to the
526 major helical axis, Csd5 may sense curvature. Alternatively, the C-terminal SH3 domain
527 of Csd5 can bind to PG directly (Blair *et al.*, 2018) and may sense a particular curvature
528 or structure of the cell wall.

529 In addition to understanding how the helical cell shape of *H. pylori* is controlled,
530 this study provides information about how CcmA and potentially other bactofilins function.

531 Modeling combined with circular dichroism data show that the bactofilin domain is a β-
532 helix and the two short terminal regions are largely unstructured. Additionally, we
533 identified that two previously studied CcmA point mutants that cause loss of function are
534 unfolded (Figure 3). The I55 and L110 residues are homologous to residues mutated by
535 Vasa and colleagues in BacA (V75 and F130 in BacA) and are predicted to reside in the
536 interior of the hydrophobic core of the proteins and mutating these residues destabilizes
537 the proteins likely through the hydrophobic effect (Taylor *et al.*, 2020; Vasa *et al.*, 2015).
538 We also identified that the bactofilin domain is capable of polymerizing on its own, the N-
539 terminal region promotes lateral interactions between filaments, and the N- and C-
540 terminal regions are both necessary for lattice formation. These data correlate with what
541 has been previously reported in the literature; in the bactofilin Ttbac from *T. thermophilus*
542 loss of the N-terminal region (residues 1-10 in Ttbac) generated smaller, more ordered
543 bundles of filaments (Deng *et al.*, 2019), and it has been previously reported that purified
544 Δ*CT* CcmA from *H. pylori* does not form lattice structures (Holtrup *et al.*, 2019).

545 In this study, we identified several putative functional motifs within CcmA. The N-
546 terminal region (amino acids 1-18) is important for patterning helical cell shape and
547 regulates interactions with Csd7, suggesting that the N-terminal region is a functional
548 motif. Our data also suggest that amino acids 13-17 in the N-terminal region of CcmA
549 promote lateral interactions between filaments *in vitro* and may be another functional
550 motif. However, in CcmA, the putative membrane binding motif (amino acids 3-12)
551 suggested by Deng and colleagues (Deng *et al.*, 2019), did not show any clear function.
552 Additionally, the C-terminal region of CcmA is not required for any of the cellular
553 phenotypes assayed (cell shape, Csd5 or Csd7 interactions, Csd1 stabilization).

554 Bactofilins are commonly found as part of complexes in other bacteria and help
555 spatially organize cells to regulate where certain functions occur (Sichel & Salama, 2020;
556 Surovtsev & Jacobs-Wagner, 2018). Our findings regarding how CcmA functions within
557 a complex in *H. pylori* provides insight into how bactofilins operate within complexes in
558 other bacterial species. Mechanisms similar to how CcmA functions in *H. pylori* have been
559 reported in other systems; in *A. biprostecum* a PG hydrolase, SpmX, directs the bactofilin
560 BacA to the site of stalk synthesis, then BacA organizes the rest of the complex (Caccamo
561 *et al.*, 2020) to control stalk morphogenesis. Here, we identified that CcmA is not capable
562 of localizing to the cell envelope without Csd5. While Csd5 is unique to the *Helicobacter*
563 genus, transmembrane proteins in other species may also be essential for localization of
564 bactofilins. Interestingly, the genomic arrangement of *csd1* (an M23 metallopeptidase)
565 and *CcmA* overlapping is conserved in several other curved and helical species of
566 Campylobacterota and Pseudomonadota (Billini *et al.*, 2019; Caccamo *et al.*, 2020;
567 Sycuro *et al.*, 2010), and has been reported in a spirochete (Jackson *et al.*, 2018),
568 suggesting that bactofilins may regulate M23 metallopeptidases to promote PG
569 remodeling at specific regions of the cell envelope to control cell shape and
570 morphogenesis of other morphological features. Our work is the first to suggest a
571 mechanism by which a bactofilin can regulate a PG hydrolase indirectly through a
572 transmembrane membrane protein and protein stability.
573
574
575
576 <u>Materials and Methods</u>

577

578 **Bacterial strains and growth**

579 Strains used in this work, as well as primers and plasmids used in strain construction are
580 available in the appendix. *H. pylori* was grown in Brucella Broth (BD) supplemented with
581 10% heat-inactivated fetal bovine serum (Cytiva Hyclone) without antimicrobials or on
582 horse blood agar plates with microbials as described (Sycuro *et al.*, 2010). For resistance
583 marker selection, horse blood agar plates were supplemented with 15 µg/ml
584 chloramphenicol, 25 µg/ml kanamycin, or 60 mg/ml sucrose. *H. pylori* strains were grown
585 at 37 °C under micro-aerobic conditions in a tri-gas incubator (10% CO_2, 10% O_2, and
586 80% N_2). For plasmid selection and maintenance in *E. coli,* cultures were grown in
587 Lysogeny broth (LB) or on LB-agar at 37 °C supplemented with 100 µg/mL ampicillin or
588 25 µg/ml Kanamycin.

589

590 **Protein structure prediction**

591 Swiss-Model was used to identify the boundaries between the bactofilin domain and the
592 terminal regions of CcmA. The primary amino acid sequence of CcmA from the *H. pylori*
593 G27 genome (GenBank: CP001173.1) was submitted to Swiss-Model
594 (https://swissmodel.expasy.org/ (Waterhouse *et al.*, 2018)) where the structure of BacA
595 from *C. crescentus* (Vasa *et al.*, 2015) was used to model CcmA. RoseTTAFold was used
596 to predict the structure of CcmA; the same primary amino acid sequence of CcmA was
597 submitted to the Robetta protein prediction service (https://robetta.bakerlab.org/ (Baek *et*
598 *al.*, 2021)). Models generated in RoseTTAFold were modified in Pymol (The PyMOL
599 Molecular Graphics System, Version 2.4.2 Schrödinger, LLC.).

600

601 **Western blotting**

602 Whole cell extracts of *H. pylori* were prepared by harvesting 1.0 optical density at 600 nm
603 (OD_{600}) of log phase liquid culture (0.3-0.7 OD_{600}) by centrifugation for 2 minutes. Then,
604 bacteria were resuspended to a concentration of 10 OD_{600} per ml with 2x protein sample
605 buffer (0.1 M Tris-HCl, 4% SDS, 0.2% bromophenol blue, 20% glycerol) with or without
606 5% β-mercaptoethanol (BME). Samples were loaded onto Mini-PROTEAN TGX 4-15%
607 polyacrylamide gels (Bio-Rad) and transferred onto polyvinylidene difluoride (PVDF)
608 membranes using the Trans-Blot TurboTransfer System (Bio-Rad) system. Membranes
609 were either stained with 0.1% Ponceu S solution in 5% acetic acid (Sigma) first, or
610 immediately blocked for 2 hours at room temperature in 5% non-fat milk in tris-buffered
611 saline containing 0.05% tween-20 (TBS-T) then incubated either overnight at 4 °C or at
612 room temperature for 1 hour with primary antibodies, 1:10,000 for α-CcmA (Blair et al.,
613 2018), 1:5,000 for α-FLAG (M2, Sigma), 1:10,000 for α-Csd1 (Yang *et al.*, 2019), 1:20,000
614 for α-cag3 (Pinto-Santini & Salama, 2009), or 1:10,000 for α-Csd1 (Promega). Then
615 washed 5 times with TBS-T over a 30-minute period, incubated with secondary antibodies
616 for 1 hour at room temperature at 1:20,000 with appropriate horseradish peroxidase-
617 conjugated α-immunoglobulin antibodies (α-rabbit for CcmA Csd1, or Cag3; α-mouse for
618 FLAG, Santa Cruz Biotechnology), then washed 5 times with TBS-T over a 30-minute
619 period. Proteins were detected using a chemiluminescent substrate according to
620 manufacturer's instructions (Pierce ECL substrate for standard Western blotting or
621 Immobilon Western HRP substrate (Millipore) for Western blotting following co-

622 immunoprecipitation experiments) and imaged directly with the Bio-Rad gel
623 documentation system.

624 **Western blot densitometry**

625 Western blot densitometry was performed using Image Lab software version 6.0.1 (Bio-
626 Rad). The lanes on each Western blot were defined, then the adjusted total lane volume
627 was calculated by the software. To calculate relative Csd1 levels, the signal detected by
628 the α-Csd1 antibody for each sample was divided by the signal detected by the α-Cag3
629 antibody from the same sample on the same membrane. After calculating relative Csd1
630 levels, they were normalized by dividing the signal by the relative Csd1 level from the
631 SSH51A strain (*rdxA::csd1*).

632

633 **Phase contrast microscopy and quantitative morphology analysis**

634 Phase contrast microscopy and image analysis was performed as previously described
635 (Sycuro *et al.*, 2010). Briefly, cells were grown in liquid culture to mid-log phase (0.3-0.7
636 OD_{600}), centrifuged, and resuspended in 4% paraformaldehyde (PFA) in phosphate-
637 buffered saline (PBS) and mounted on glass slides. Cells were imaged with a Nikon TE
638 200 microscope equipped with a 100X oil immersion lens objective and Photometrics
639 CoolSNAP HQ charge-coupled-device camera. Images were thresholded with FIJI
640 (Schindelin *et al*, 2012) and CellTool software (Pincus & Theriot, 2007) was used to
641 measure both side curvature and central axis length.

642

643 **Protein purification**

644 Purification of 6-his CcmA was performed exactly as described previously (Taylor *et al.*,
645 2020). *E. coli* strains used to recombinantly express CcmA were: pKB62A in BL21 DE3,
646 pSS15A in BL21 DE3, pSS16A in BL21 DE3, pSS17A in BL21 DE3, pSS18B in BL21
647 DE3, pSS19A in BL21 DE3, pKB69H in BL21 DE3, and pKB72D in BL21 DE3 and are
648 described in detail in the appendix.
649
650 **Circular dichroism**
651 After purification of 6-his CcmA, samples were dialyzed against 10 mM CAPS pH 11 at a
652 volume of 1:10,000 for 24 hours, then the buffer was changed, and dialysis continued for
653 another 24 hours. After dialysis was complete, samples were normalized to 0.5 mg/ml.
654 CD spectra were collected from 180-260 nm while holding the temperature constant with
655 a Jasco J-815 Circular Dichroism Spectropolarimeter.
656
657 **Negative stain and Transmission Electron Microscopy (TEM)**
658 After purification of 6-his CcmA samples were dialyzed against 25 mM Tris pH 8 for 24
659 hours. Samples were then normalized to 1 mg/ml and placed on carbon-coated grids after
660 glow-discharging. Samples were fixed in ½ X Karnovsky's fixative and washed with 0.1
661 M Cacodylate buffer and water, then stained with Nano-W (Nanoprobes) for 60 seconds,
662 wicked, then stained for another 60 seconds. Images were acquired on a kV
663 ThermoFisher Talos 120C LaB_6 microscope equipped with a Ceta Camera using Leginon
664 software (Suloway *et al*, 2005). The width of bundles and filaments were measured using
665 FIJI (Schindelin *et al.*, 2012).
666

667 **Co-immunoprecipitation experiments**

668 Co-immunoprecipitation experiments were performed as previously described in Blair *et*
669 *al.,* 2018 and Yang *et al.,* 2019 with slight modifications. *H. pylori* expressing FLAG tags
670 fused to either Csd5 or Csd7 were grown to mid-log phase in liquid culture and 15 OD_{600}
671 were harvested by centrifugation at 10,000 RPM for 10 minutes at 4 °C. Cells pellets were
672 resuspended in 1.8 ml of cold lysis buffer (20 mM tris pH 8, 150 mM NaCl, 2% glycerol,
673 1% Triton X-100 and EDTA-free protease inhibitor (Pierce)). The cells were sonicated at
674 10% power for 10 second intervals with a microtip (Sonic Dismembrator Model 500,
675 Branson) until visibly cleared, then centrifuged at 20,000 RCF for 30 minutes at 4 °C. The
676 soluble fraction was then incubated with 40 µl beads (α-FLAG M2 agarose beads
677 (Sigma)) or α-VSV-G agarose beads (Sigma) equilibrated in wash buffer (20 mM tris pH
678 8, 150 mM NaCl, 2% glycerol, 0.1% Triton X-100) for 90 minutes at 4 °C. The beads were
679 then washed four times in 10 ml cold wash buffer, samples were centrifuged at 2000 RPM
680 for 2 minutes between washes. Beads were then boiled in 45 µl 2x sample buffer without
681 BME for 10 minutes and subjected to Western blotting.

682

683 **Labeling with fluorescent WGA and HaloTag ligands**

684 *H. pylori* expressing CcmA-HaloTag were grown to mid-log phase and fixed with 4% PFA
685 for 45 minutes at room temperature. After fixing, bacteria were permeabilized for 1 hour
686 at room temperature with PBS + 0.05% Triton X-100. Bacteria were then resuspended in
687 PBS and centrifuged onto #1.5 coverslips. Next, coverslips were incubated on a droplet
688 of PBS containing 30 µg/ml af488-conjucated WGA (Invitrogen) and 4 µM JF-549
689 (Promega) for 30 minutes at room temperature. Coverslips were washed four times (10

690 minutes each) by placing on fresh droplets of PBS + 0.1% Tween-20, then mounted on
691 glass slides with ProLong Diamond Antifade Mountant (Invitrogen).
692
693 **3D Structured Illumination Microscopy**
694 3D structured illumination microscopy (SIM) was performed on a DeltaVIsion OMX SR
695 equipped with PCO scientific CMOS cameras, 488 nm and 568 nm lasers, and an
696 Olympus 60X/1.42 U PLAN APO oil objective with oil matched for the sample refractive
697 index. 512 x 512 pixel Z-stack images were acquired with 125 nm spacing and 3 μm total
698 thickness. Figures were generated by changing channel colors, adjusting brightness and
699 contrast in FIJI, brightness and contrast settings were maintained across the entire image
700 (Schindelin *et al.*, 2012). Figures were assembled in Adobe Illustrator.
701
702 **3D reconstructions and curvature enrichment analysis**
703 3D reconstructions were generated, and curvature CcmA enrichment analysis was
704 preformed exactly as described in Taylor *et al.,* 2020 using existing software (Bratton *et*
705 *al.*, 2019; Bratton *et al*, 2018). Briefly, 3D SIM Z-stack images were used to generate a
706 3D triangular meshwork surface with roughly 30 nm precision from the WGA channel.
707 After generating the 3D triangular meshwork, the Gaussian curvature was calculated at
708 every location on the surface of the cell and we performed curvature enrichment analysis
709 to identify which GC values CcmA signal was associated with where uniform signal=1.
710 Because the absolute amount of CcmA signal can differ between cells and because the
711 illumination throughout the field is non-uniform, we set the average CcmA signal on each
712 cell as one. Then we measured each cell's curvature dependent CcmA signal intensity

713 relative to one, normalized by the amount of the curvature present on that individual cell
714 surface.
715
716 **Analysis of intensity of CcmA-HaloTag signal at cell surface and within cells**
717 A custom Matlab script was used to compute the relative intensity of CcmA-HaloTag
718 signal at the cell surface and at surfaces generated by shrinking the surface of interest
719 toward the centerline of the cell (negative offsets) or increasing the surface away from the
720 centerline (positive offsets). For each of these shells, or surface offsets, we calculated the
721 average WGA signal and the average CcmA-HaloTag signal. To account for errors in
722 spatial alignment between the two color channels, before calculating the intensity at each
723 shell, we performed a rigid body alignment procedure to maximize the intensity of the
724 signal contained within the nominal reconstructed surface (0 nm offset). Consistent with
725 the fact that we utilized the WGA channel for shape reconstructions, this alignment
726 algorithm returned offsets of less than one pixel for the WGA channel. The CcmA-
727 HaloTag channel showed more variability in the offsets, sometimes requiring an offset of
728 almost 200 nm along the focal direction, consistent with small, wavelength dependent
729 variations in focal position. After calculating the average intensity at each subshell, or
730 resized surface, we normalized the highest concentration to 1 before averaging across
731 all the cells in our sample.
732
733 Acknowledgements
734 This research was supported by the US National Institute of Heath (NIH) grants
735 F31 AI152331 (SRS), T32 GM95421 (SRS), R01 AI136946 (NRS). As well as the GO-

MAP Graduate Opportunity Program Research Assistantship award (GOP Award) (SRS) and the VUMC Discovery Scholars in Health and Medicine Program (BPB). This research was supported by the Genomics and Cellular Imaging and Electron Microscopy shared resources of the Fred Hutch/University of Washington Cancer Consortium (P30 CA015704). The opinions, findings, and conclusions or recommendations expressed in this material contents are solely the responsibility of the authors and do not necessarily represent the official views of the NIH.

We would like to thank Joseph Stembel (University of Washington) for construction of strains JS02 and JS09, Jennifer Taylor (University of Washington) for helpful advice and training, Ethan Garner (Harvard) for helpful discussion, James McDermott for thoughtful discussion and review of this manuscript, David Baker and Justin Decarreau (University of Washington), and the support of the Audacious Project at the Institute for Protein Design for use of the DeltaVision OMX microscope, Roland Strong and Barry Stoddard (Fred Hutchinson Cancer Center) for use of the Circular Dichroism Spectropolarimeter, and Caleigh Azumaya (Fred Hutchinson Cancer Center) for assistance with the Talos microscope.

Data Availability

The datasets and computer code produced in this study will be available soon at the following locations:

- Matlab scripts and documentation: https://github.com/PrincetonUniversity/shae-cellshape-public.
- Imaging datasets: https://www.ebi.ac.uk/bioimage-archive/

759

760 Author contributions

761 Conception and design of the study (SRS, NRS), acquisition of data (SRS), analysis and
762 interpretation of data (SRS, NRS, BPB), writing the manuscript (SRS, NRS).

763

764 Conflict of interest

765 The authors have no conflicts of interest to report.

766

767 References

768 Asmar AT, Ferreira JL, Cohen EJ, Cho SH, Beeby M, Hughes KT, Collet JF (2017)
769 Communication across the bacterial cell envelope depends on the size of the periplasm.
770 *PLoS Biol* 15: e2004303

771 Baek M, DiMaio F, Anishchenko I, Dauparas J, Ovchinnikov S, Lee GR, Wang J, Cong
772 Q, Kinch LN, Schaeffer RD *et al* (2021) Accurate prediction of protein structures and
773 interactions using a three-track neural network. *Science* 373: 871-876

774 Billini M, Biboy J, Kuhn J, Vollmer W, Thanbichler M (2019) A specialized MreB-
775 dependent cell wall biosynthetic complex mediates the formation of stalk-specific
776 peptidoglycan in Caulobacter crescentus. *PLoS Genet* 15: e1007897

777 Blair KM, Mears KS, Taylor JA, Fero J, Jones LA, Gafken PR, Whitney JC, Salama NR
778 (2018) The Helicobacter pylori cell shape promoting protein Csd5 interacts with the cell
779 wall, MurF, and the bacterial cytoskeleton. *Mol Microbiol* 110: 114-127

780 Bratton BP, Barton B, Morgenstein RM (2019) Three-dimensional Imaging of Bacterial
781 Cells for Accurate Cellular Representations and Precise Protein Localization. *J Vis Exp*

782 Bratton BP, Shaevitz JW, Gitai Z, Morgenstein RM (2018) MreB polymers and curvature
783 localization are enhanced by RodZ and predict E. coli's cylindrical uniformity. *Nat*
784 *Commun* 9: 2797

785 Brockett MR, Lee J, Cox JV, Liechti GW, Ouellette SP (2021) A Dynamic, Ring-Forming
786 Bactofilin Critical for Maintaining Cell Size in the Obligate Intracellular Bacterium
787 Chlamydia trachomatis. *Infect Immun* 89: e0020321

788 Bulyha I, Lindow S, Lin L, Bolte K, Wuichet K, Kahnt J, van der Does C, Thanbichler M,
789 Sogaard-Andersen L (2013) Two small GTPases act in concert with the bactofilin
790 cytoskeleton to regulate dynamic bacterial cell polarity. *Dev Cell* 25: 119-131

791 Caccamo PD, Jacq M, VanNieuwenhze MS, Brun YV (2020) A Division of Labor in the
792 Recruitment and Topological Organization of a Bacterial Morphogenic Complex. *Curr Biol*
793 30: 3908-3922 e3904

794 Chang YW, Shaffer CL, Rettberg LA, Ghosal D, Jensen GJ (2018) In Vivo Structures of
795 the Helicobacter pylori cag Type IV Secretion System. *Cell Rep* 23: 673-681

796 de Martel C, Georges D, Bray F, Ferlay J, Clifford GM (2020) Global burden of cancer
797 attributable to infections in 2018: a worldwide incidence analysis. *The Lancet Global*
798 *Health* 8: e180-e190

799 Deng X, Gonzalez Llamazares A, Wagstaff JM, Hale VL, Cannone G, McLaughlin SH,
800 Kureisaite-Ciziene D, Lowe J (2019) The structure of bactofilin filaments reveals their
801 mode of membrane binding and lack of polarity. *Nat Microbiol* 4: 2357-2368

802 El Andari J, Altegoer F, Bange G, Graumann PL (2015) Bacillus subtilis Bactofilins Are
803 Essential for Flagellar Hook- and Filament Assembly and Dynamically Localize into
804 Structures of Less than 100 nm Diameter underneath the Cell Membrane. *PLoS One* 10:
805 e0141546

806 Greenfield NJ (2006) Using circular dichroism spectra to estimate protein secondary
807 structure. *Nat Protoc* 1: 2876-2890

808 Hay NA, Tipper DJ, Gygi D, Hughes C (1999) A Novel Membrane Protein Influencing Cell
809 Shape and Multicellular Swarming of Proteus mirabilis. *Journal of*
810 *Bacteriology* 181: 2008-2016

811 Holtrup S, Heimerl T, Linne U, Altegoer F, Noll F, Waidner B (2019) Biochemical
812 characterization of the Helicobacter pylori bactofilin-homolog HP1542. *PLoS One* 14:
813 e0218474

814 Hooi JKY, Lai WY, Ng WK, Suen MMY, Underwood FE, Tanyingoh D, Malfertheiner P,
815 Graham DY, Wong VWS, Wu JCY *et al* (2017) Global Prevalence of Helicobacter pylori
816 Infection: Systematic Review and Meta-Analysis. *Gastroenterology* 153: 420-429

817 Hrast M, Turk S, Sosic I, Knez D, Randall CP, Barreteau H, Contreras-Martel C, Dessen
818 A, O'Neill AJ, Mengin-Lecreulx D *et al* (2013) Structure-activity relationships of new

819 cyanothiophene inhibitors of the essential peptidoglycan biosynthesis enzyme MurF. *Eur*
820 *J Med Chem* 66: 32-45

821 Huang KC, Mukhopadhyay R, Wen B, Gitai Z, Wingreen NS (2008) Cell shape and cell-
822 wall organization in Gram-negative bacteria. *Proc Natl Acad Sci U S A* 105: 19282-19287

823 Jackson KM, Schwartz C, Wachter J, Rosa PA, Stewart PE (2018) A widely conserved
824 bacterial cytoskeletal component influences unique helical shape and motility of the
825 spirochete Leptospira biflexa. *Mol Microbiol* 108: 77-89

826 Koch MK, McHugh CA, Hoiczyk E (2011) BacM, an N-terminally processed bactofilin of
827 Myxococcus xanthus, is crucial for proper cell shape. *Mol Microbiol* 80: 1031-1051

828 Kuhn J, Briegel A, Morschel E, Kahnt J, Leser K, Wick S, Jensen GJ, Thanbichler M
829 (2010) Bactofilins, a ubiquitous class of cytoskeletal proteins mediating polar localization
830 of a cell wall synthase in Caulobacter crescentus. *EMBO J* 29: 327-339

831 Lin L, Osorio Valeriano M, Harms A, Sogaard-Andersen L, Thanbichler M (2017)
832 Bactofilin-mediated organization of the ParABS chromosome segregation system in
833 Myxococcus xanthus. *Nat Commun* 8: 1817

834 Lu P, Zhang H, Gao Y, Jia X, Liu Z, Wang D, Au SWN, Zhang Q (2022) Cryo-electron
835 Tomography Reveals the Roles of FliY in Helicobacter pylori Flagellar Motor Assembly.
836 *mSphere* 7: e0094421

837 Martinez LE, O'Brien VP, Leverich C, Knoblaugh SE, Salama NR (2018) Non-helical
838 Helicobacter pylori show altered gland colonization and elicit less gastric pathology during
839 chronic infection. *bioRxiv*: 505107

840 Montecucco C, Rappuoli R (2001) Living dangerously: how Helicobacter pylori survives
841 in the human stomach. *Nat Rev Mol Cell Biol* 2: 457-466

842 Osorio-Valeriano M, Altegoer F, Steinchen W, Urban S, Liu Y, Bange G, Thanbichler M
843 (2019) ParB-type DNA Segregation Proteins Are CTP-Dependent Molecular Switches.
844 *Cell* 179: 1512-1524 e1515

845 Pincus Z, Theriot JA (2007) Comparison of quantitative methods for cell-shape analysis.
846 *J Microsc* 227: 140-156

847 Pinto-Santini DM, Salama NR (2009) Cag3 is a novel essential component of the
848 Helicobacter pylori Cag type IV secretion system outer membrane subcomplex. *J*
849 *Bacteriol* 191: 7343-7352

850 Qin Z, Lin WT, Zhu S, Franco AT, Liu J (2017) Imaging the motility and chemotaxis
851 machineries in Helicobacter pylori by cryo-electron tomography. *J Bacteriol* 199: e00695-
852 00616

853 Schindelin J, Arganda-Carreras I, Frise E, Kaynig V, Longair M, Pietzsch T, Preibisch S,
854 Rueden C, Saalfeld S, Schmid B *et al* (2012) Fiji: an open-source platform for biological-
855 image analysis. *Nat Methods* 9: 676-682

856 Sichel SR, Salama NR (2020) Bacterial Cell Biology: It Takes Two to Tango. *Curr Biol* 30:
857 R1258-R1260

858 Smeets LC, Bijlsma JJ, Boomkens SY, Vandenbroucke-Grauls CM, Kusters JG (2000)
859 comH, a novel gene essential for natural transformation of Helicobacter pylori. *J Bacteriol*
860 182: 3948-3954

861 Suloway C, Pulokas J, Fellmann D, Cheng A, Guerra F, Quispe J, Stagg S, Potter CS,
862 Carragher B (2005) Automated molecular microscopy: the new Leginon system. *J Struct*
863 *Biol* 151: 41-60

864 Surovtsev IV, Jacobs-Wagner C (2018) Subcellular Organization: A Critical Feature of
865 Bacterial Cell Replication. *Cell* 172: 1271-1293

866 Sycuro LK, Pincus Z, Gutierrez KD, Biboy J, Stern CA, Vollmer W, Salama NR (2010)
867 Peptidoglycan crosslinking relaxation promotes Helicobacter pylori's helical shape and
868 stomach colonization. *Cell* 141: 822-833

869 Sycuro LK, Rule CS, Petersen TW, Wyckoff TJ, Sessler T, Nagarkar DB, Khalid F, Pincus
870 Z, Biboy J, Vollmer W *et al* (2013) Flow cytometry-based enrichment for cell shape
871 mutants identifies multiple genes that influence Helicobacter pylori morphology. *Mol*
872 *Microbiol* 90: 869-883

873 Sycuro LK, Wyckoff TJ, Biboy J, Born P, Pincus Z, Vollmer W, Salama NR (2012) Multiple
874 peptidoglycan modification networks modulate Helicobacter pylori's cell shape, motility,
875 and colonization potential. *PLoS Pathog* 8: e1002603

Taylor JA, Bratton BP, Sichel SR, Blair KM, Jacobs HM, DeMeester KE, Kuru E, Gray J, Biboy J, VanNieuwenhze MS *et al* (2020) Distinct cytoskeletal proteins define zones of enhanced cell wall synthesis in Helicobacter pylori. *Elife* 9

Vasa S, Lin L, Shi C, Habenstein B, Riedel D, Kuhn J, Thanbichler M, Lange A (2015) beta-Helical architecture of cytoskeletal bactofilin filaments revealed by solid-state NMR. *Proc Natl Acad Sci U S A* 112: E127-136

Waterhouse A, Bertoni M, Bienert S, Studer G, Tauriello G, Gumienny R, Heer FT, de Beer TAP, Rempfer C, Bordoli L *et al* (2018) SWISS-MODEL: homology modelling of protein structures and complexes. *Nucleic Acids Res* 46: W296-W303

Yang DC, Blair KM, Taylor JA, Petersen TW, Sessler T, Tull CM, Leverich CK, Collar AL, Wyckoff TJ, Biboy J *et al* (2019) A Genome-Wide Helicobacter pylori Morphology Screen Uncovers a Membrane-Spanning Helical Cell Shape Complex. *Journal of Bacteriology* 201: e00724-00718

Supplemental Figures

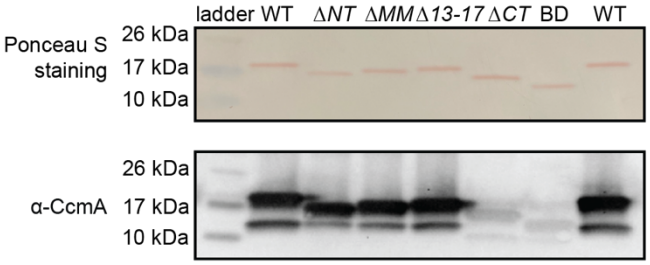

894 Supplemental Figure 1- Robust CcmA detection with α-CcmA polyclonal antibody
895 requires the C-terminus. 0.1 µg of purified protein was loaded into each lane. Top row:
896 Ponceau S staining of purified 6-his-CcmA. Bottom Row: Western blot probed with
897 polyclonal α-CcmA antibody, both images are of the same membrane.

898

899

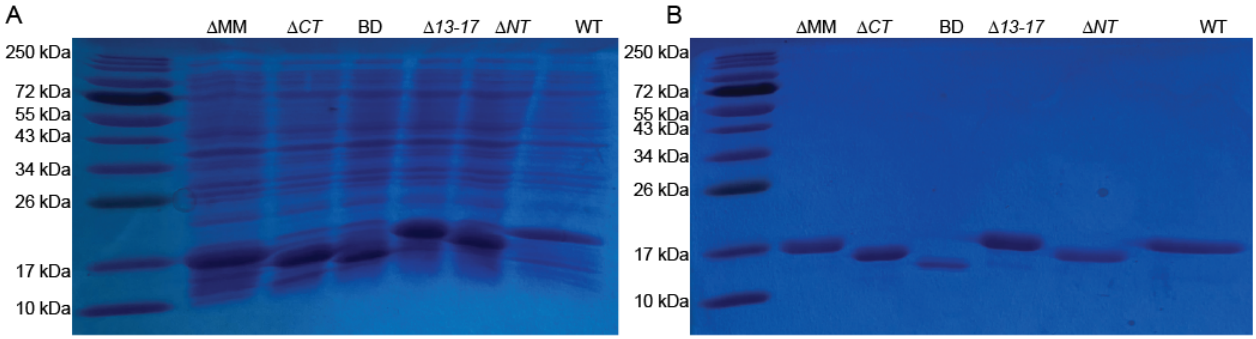

900

901 Supplemental Figure 2- Purification of WT and mutant 6-his CcmA. (A) Coomassie-
902 stained gel of induced, whole cell lysates of *E. coli*. (B) Coomassie-stained gel of the first
903 elution after purification of 6-his CcmA with cobalt affinity resin.

904

905

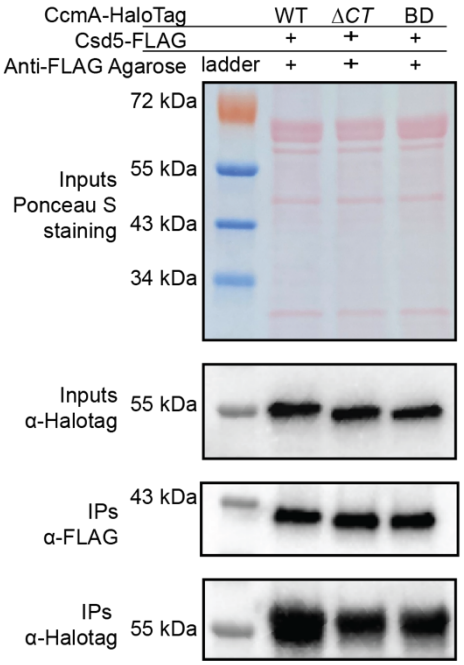

Supplemental Figure 3- The C-terminus of CcmA-HaloTag is not required for interactions with Csd5. α-FLAG immunoprecipitation of strains expressing Csd5-FLAG and WT CcmA-HaloTag, CcmA Δ*CT*-HaloTag, or CcmA BD only -HaloTag. Top Row: Ponceau S staining of input fractions. Second row: Western blot of inputs probed with α-HaloTag monoclonal antibody to detect CcmA-HaloTag, both top and second row are images of the same membrane. Third row: Western blot of IP fractions probed with α-FLAG monoclonal antibody to detect Csd5-FLAG. Bottom row: Western blot of IP fractions probed with α-HaloTag monoclonal antibody to detect CcmA-HaloTag. Strains used: SSH87A, SSH89A, and SSH97A

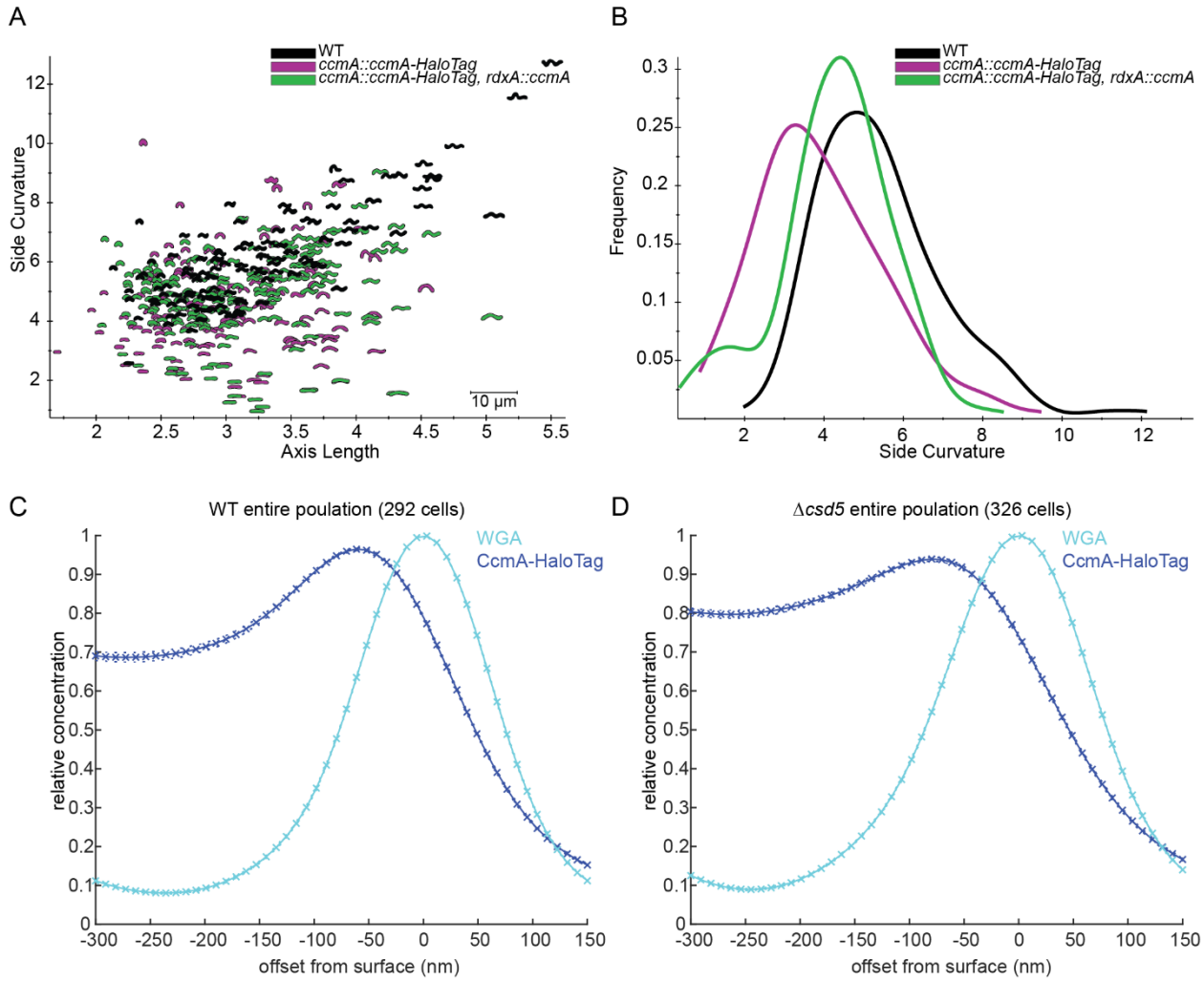

Supplemental Figure 4- Cell shape of CcmA-HaloTag strains and analysis of CcmA-HaloTag surface signal in populations. (A) Scatterplot of outlines of *H. pylori* cells derived from phase contrast images. (B) Histogram displaying side curvature of each population. WT (LSH100) n=116 cells, *ccmA::ccmA-Halotag* (SSH38A) n=133 cells, *ccmA::ccmA-HaloTag, rdxA::ccmA* (SSH39B) n=190 cells. (C-D) Plots displaying the relative concentration of HaloTag-CcmA and WGA signal at the cell surface (X=0 nm) and at computationally generated cell surfaces that are inside (X<0 nm) and outside (X>0 nm) of the cell surface. Crosses indicate SEM. Populations of WT (C) and Δ*csd5* (D) cells from three independent experiments were pooled.